DIFFRACTION IMAGING BASED ON THE DIFFRACTION OPERATOR

J.J.S. Figueiredo, F. Oliveira, E. Esmi, L. Freitas, A. Novais, and J. Schleicher

email: *jadsomjose@gmail.com*

keywords: *Diffraction operator, Kirchhoff migration, kNN classifier, diffraction imaging*

ABSTRACT

Seismic diffractions carry detailed structure information. Therefore, the development of computational resources capable of detecting diffractor points with a good resolution is desirable, but has been a challenge in the area of seismic processing. In this work, we present two approaches to seismic diffraction imaging based on the diffraction operator, which can be used in both the time and depth domains, in accordance with the complexity of the area. The first method makes applies pattern recognition to the amplitudes along the diffraction operator. The second method relies on a statistical analysis of these amplitudes to design a weight function that suppresses noise and reflections and enhances diffraction events. Numerical examples demonstrate the feasibility of both techniques and compare their results.

INTRODUCTION

Diffracted waves have played an important role to determine certain kinds of complex geological structures. Some of these structures are well-known as common hydrocarbon traps, such as faults, pinch-outs, unconformities and structures the size of which is in the order of the wavelength (Halliburton, 2001).

Because of the importance of these types of structures, several methods for imaging diffractions have been developed in the recent past. The first authors to look into the topic were Landa et al. (1987) and Landa and Keydar (1998), who proposed and refined a detection method related to specific kinematic and dynamic properties of diffracted waves. Another approach (Moser and Howard, 2008) is based on suppressing specular reflections to image diffractions in the depth domain. Most recently, Zhu and Wu (2010) developed a method based on the local image matrix (LIM), which uses an imaging condition in the local incident and reflection angles for source-receiver pairs to detect diffractions.

In this work, we propose two diffraction detection methods based on an amplitude analysis along the elementary diffractions (Tabti et al., 2004). The present methods do not require any knowledge apart of from the migration velocity field, i.e., rms velocities or interval velocities depending of the complexity of the area. The first method makes applies pattern recognition to the amplitudes along the diffraction operator. The second method relies on a statistical analysis of these amplitudes to design a weight function that suppresses noise and reflections and enhances diffraction events. Numerical examples demonstrate the feasibility of both techniques and compare their results.

THEORY

Diffraction operator

Tabti et al. (2004) introduced amplitude analysis along elementary diffractions for Fresnel aperture specification. As illustrated in Figure 1a, the traveltime of an elementary diffraction associated with a reflection point is tangent to the reflection traveltime at the stationary point (location of the specular reflection event).

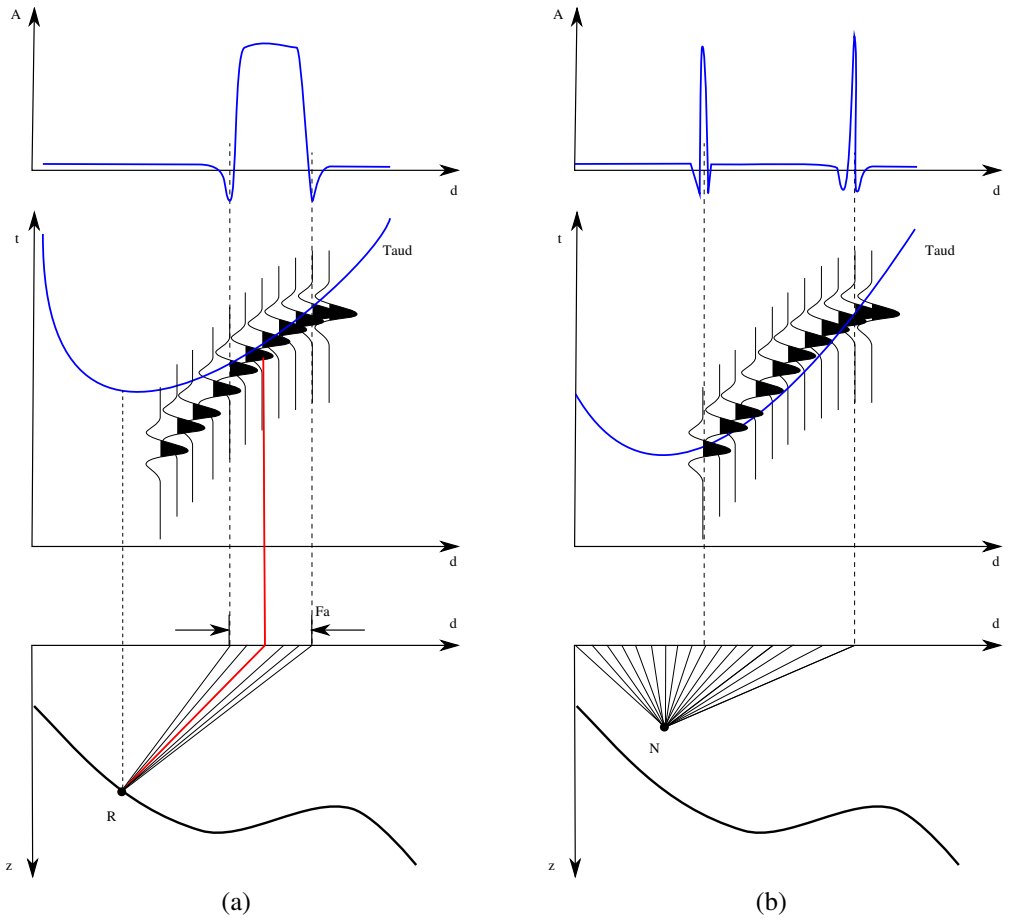

Figure 1: Illustration of the diffraction operator for (a) a reflection point and (b) a void image point. Top: amplitude along the diffraction operator; center: diffraction traveltime and seismic event; bottom: image point and ray family.

More specifically, in limited bandwidth situations, this tangential point becomes a tangential contact region, which defines the minimum aperture for true-amplitude Kirchhoff migration (Schleicher et al., 1997). Tabti et al. (2004) named it the Fresnel aperture due to its close relationship to the Fresnel zone. For image point off any reflectors or diffractors, below referred to as "void image points", there is no such region. The traveltime of the elementary diffraction associated with a void image point may cross some reflection events, but won't be tangential to any events (see Figure 1b), except for extremely rare coincidental situations.

Tabti et al. (2004) described amplitude analysis along elementary diffractions by means of a diffraction operator $\mathcal{D}$. This operator derives from the Kirchhoff depth migration integral (see, e.g., Schleicher et al., 1993)

$$I(M) = \iint\limits_{A_f} d^2\xi \; W(M,\xi)\partial_t U(\xi,t)|_{t=\tau_D(M,\xi)} \tag{1}$$

where $U(\xi,t)$ is the seismic data measured at ξ, $\tau_D(M,\xi)$ is the traveltime of the elementary diffraction of M, A_f is the Fresnel aperture, and $W(M,\xi)$ is a weight function. For simplicity, we omit the weight function in the present study, i.e. $W(M,\xi) = 1$. Integration variable ξ is the horizontal coordinate of the seismic section to be migrated, for instance the midpoint coordinate for a common-offset section or the receiver coordinate for a common-shot section.

Instead of performing the summation, the diffraction operator $\mathcal{D}(M)$ at an image point M collects a single valued curve (or surface, in the 3D case), defined as a function of the integration variable ξ, whose value at ξ is the amplitude the stack in equation (1) will consider at ξ. This value defines the amplitude of

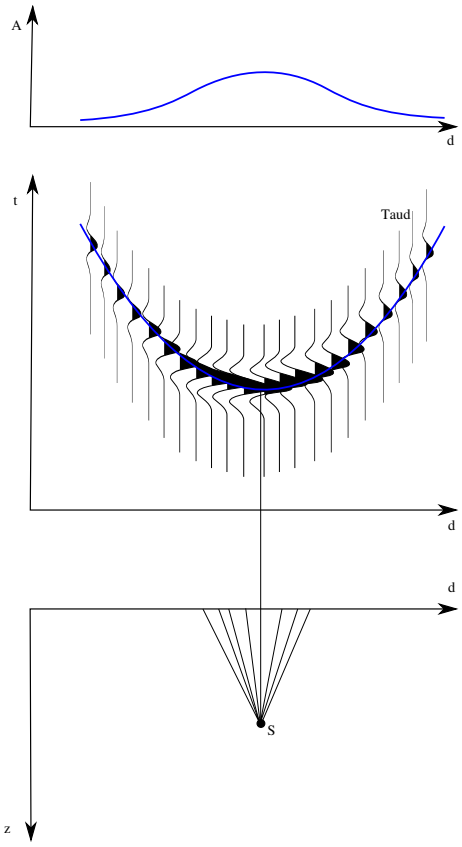

Figure 2: Illustration of the diffraction operator for a diffraction point. Top: amplitude along the diffraction operator; center: diffraction traveltime and seismic event; bottom: image point and ray family.

the elementary diffraction measured at ξ. More specifically,

$$\mathcal{D}(M,\xi) = W(M,\xi)\partial_t U(\xi,t)|_{t=\tau_D(M,\xi)} \,. \tag{2}$$

The top parts of Figure 1 represent the values of the diffraction operator $\mathcal{D}$ for the case of a reflection point (Figure 1a) and a non-reflecting point (Figure 1b).

Tabti et al. (2004) also noted that in the case of a diffractor point (either a point scatterer or an edge), the corresponding elementary diffraction corresponds to the scattered seismic event. The Fresnel aperture then extends theoretically to infinity, regardless of the frequency content of the source pulse. Figure 2 illustrates the diffraction operator at a diffraction point.

Figures 1 and 2 form the basis of both our diffraction imaging algorithms explained in the next sections. The main idea of both methods is to classify every point in the image domain M as a diffractor, reflector or noise point by means of the characteristics of its diffraction operator $\mathcal{D}(M,\xi)$. The first approach consists in a straightforward classification using a well established pattern-recognition technique called *k-nearest-neighbours* (kNN). In our second approach, we use a statistical quantity to measure how close $\mathcal{D}(M,\xi)$ is to the average pattern of a diffraction point.

Diffraction imaging by pattern recognition

Pattern recognition aims at classifying data (patterns) based either on a priori knowledge or on statistical information extracted from the patterns (Duda and Hart, 1973; Theodoridis and Koutroumbas, 1999). Pattern recognition techniques have found applications in various areas, for instance, decision making, inspection of objects, and automatic character recognition (Theodoridis and Koutroumbas, 1999).

The mathematical tool to achieve this aim is called a classifier. Suppose we are faced with the problem to classify a certain set of patterns into N classes, $w_1, \cdots, w_n$. Let $x_1, \cdots, x_p \in I\!R^n$ be samples of patterns whose class is already known, and $C_i \subseteq \{x_1, \cdots, x_p\}$ be a subset of patterns associated with class w_i such that $C_j \cap C_i = \emptyset$ for $i \neq j$, i.e., there are no subsets that fall into two different classes at the same time. Given an arbitrary pattern x, a classifier aims at associating x with one of the N classes. In this work, we are only concerned in imaging diffractions. Therefore we use two classes ($N = 2$): the diffraction class C_0 and the non-diffraction class C_1 (that includes both noise and reflection image points). We also restricted ourselves to the so-called k-nearest-neighbour (kNN) classifier, because of its simple implementation.

The kNN classifier is a supervised method to solve problems in pattern recognition. It is a method for classifying objects based on a certain distance measure and a fixed set of samples in the feature space for which the associated label of class is already known. The development of the kNN classifier was inspired by the technique for the estimation of a non-parametric probability density function (PDF) called k-nearest-neighbour density estimation, which is basically a variation of the histogram approximation of an unknown PDF. Moreover, although no assumptions about PDFs need to be made, the strategy used by the kNN model to classify patterns reminds of the well-known Bayes classification rule (Duda and Hart, 1973; Theodoridis and Koutroumbas, 1999).

Let $k \leq p$ be a positive fixed integer and $dist$ a distance measure in $I\!R^n$. Then, the kNN classification process is given by the following rules (Theodoridis and Koutroumbas, 1999)

- Find the k nearest neighbours of x in the set $\{x_1, \cdots, x_p\}$ in terms of their distances $dist(x, x_i)$, for $i = 1, \cdots, p$. Let the symbols $\tilde{x}_1, \cdots, \tilde{x}_k \in \{x_1, \cdots, x_p\}$, with $\tilde{x}_i \neq \tilde{x}_j$ for $i \neq j$, denote those k nearest neighbours.

- Identify the number k_i of patterns $\tilde{x}_i$ among these k nearest neighbours that belong to class w_i for $i = 1, \cdots, N$.

- Assign x to the class w_j with the maximum number k_j of samples.

Since the results of a kNN model depend of choice of the number k of nearest neighbours, techniques to select an appropriate parameter k like, for example, cross-validation, can be employed. Also, the performance may vary as a function of the distance measure considered. Usually, Euclidean distance is used as the distance metric.

As with all supervised models, the accuracy of the kNN classifier depends on the given training set. If non-representative samples of classes are used as training data, the performance of kNN classification can be severely degraded.

In the simulations described in the Numerical Examples section, we have employed a value of $k = 1$ and the Euclidean distance measure.

Diffraction imaging by statistical measurements

In an alternative approach to diffraction imaging, we investigate an analysis to design a stacking weight that suppresses noise and reflections and enhances diffractions. As one can easily notice, when analysing the diffraction operator at a noisy non-scattering point, the amplitude values fluctuate considerably. At a reflection point, such a fluctuation is also observed along most of the curve, except within the Fresnel aperture. On the other hand, the amplitudes along the operator evaluated at a diffraction point vary smoothly, and their fluctuation is small along a much larger portion of the curve.

As a measure of this fluctuations, at each position ξ_i of the stacking curve a local-windowed version of the standard deviation is calculated $\sigma_w(\xi_i)$. The subscript w indicates the size of the vicinity of the sample x_i in which such standard deviation is calculated, i.e., the window size. In symbols,

$$\sigma_w(\xi_i) = \sqrt{\frac{1}{2w+1} \sum_{j=i-w}^{i+w} \left[x_j - \mu_w(\xi_i)\right]^2}\,, \tag{3}$$

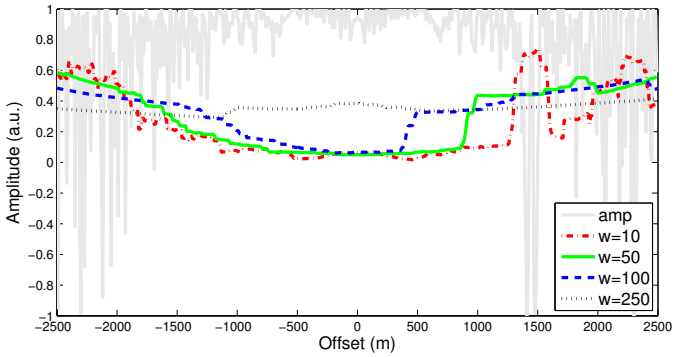

(a)

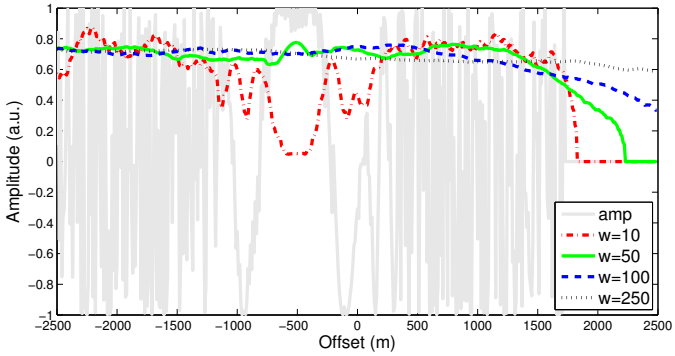

(b)

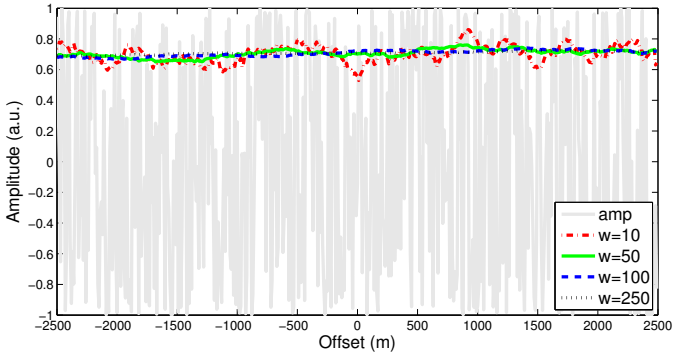

(c)

Figure 3: Amplitudes (gray lines) along diffraction curves corresponding to (a) a diffraction point, (b) a reflection point and (c) a noisy non-image point. Also shown are the values of $\sigma_w(\xi_i)$, for $w = 10$ (dot-dashed red line), 50 (solid green line), 100 (dashed blue line) and 250 (dotted black line).

where

$$\mu_w(\xi_i) = \frac{1}{2w+1} \sum_{j=i-w}^{i+w} x_j \tag{4}$$

is the mean value of all trace values $x_i = \mathcal{D}(M, \xi_i)$ within the window.

Figure 3 illustrates the behaviour of $\sigma_w(\xi_i)$ for different choices of the window length w, computed along diffraction curves representing (a) an edge diffraction point, (b) a reflection point and (c) a noisy non-scattering point. Note that there is no phase change in Figure 3 because, following a suggestion of Landa et al. (1987), we invert the signal of the amplitude at the stationary point. As expected, there are choices of w (in this case, $w \leq 50$), for which the values of σ_w at a diffraction point are low (below 0.1) for a larger interval than at a reflection point. Conversely, at a noisy non-scattering point, σ_w is high (above

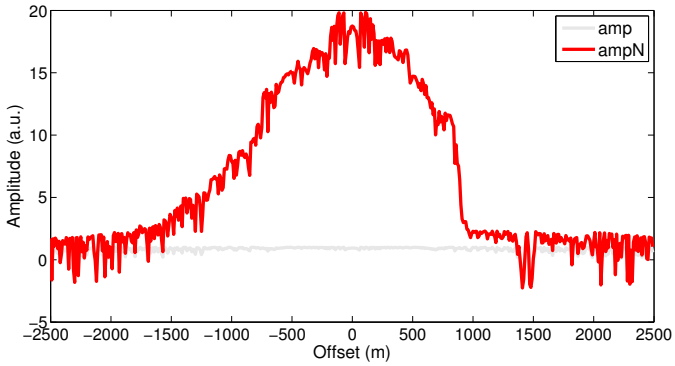

(a)

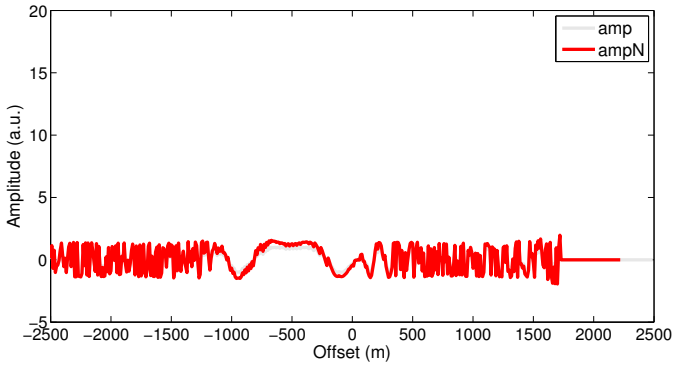

(b)

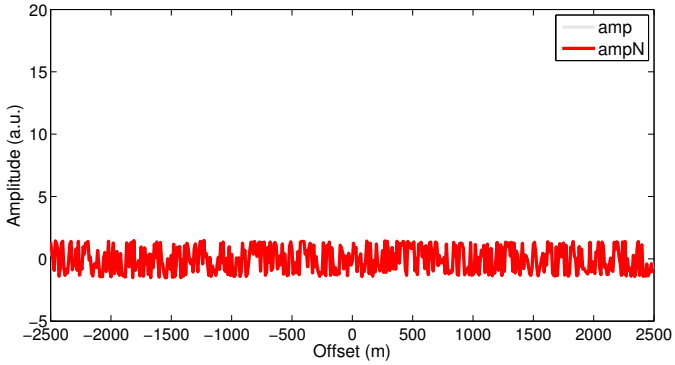

(c)

Figure 4: Amplitude curves from Figure 3 before (gray) and after (red) its normalization by means of dividing them by σ_{50}.

0.7) for the whole curve.

Using this property of the standard deviation σ_w, we can extend the approach of Landa et al. (1987) for imaging a diffraction point. For this purpose, we study the curves formed by the normalized values

$$x'_i = x_i \sqrt{n} / \sigma_w(\xi_i) \; . \tag{5}$$

These curves are plotted in Figure 4, for a (a) diffraction point, (b) reflection point and (c) noisy non-scattering point.

The three cases can then be distinguished using the different values of the area J_w^* under the curve

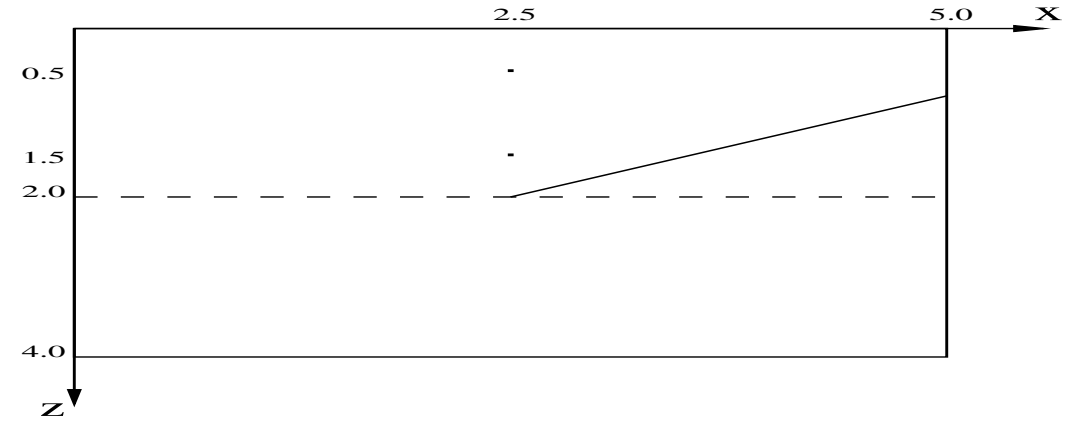

Figure 5: Model with three diffractors.

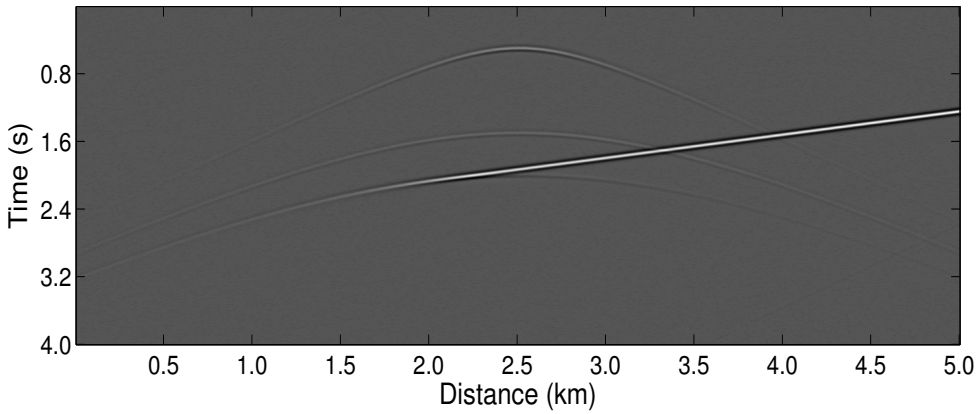

Figure 6: Zero-offset dataset generated.

formed by these normalized samples.

$$J_w^* = \frac{1}{n}\sum_{i=1}^{n} x_i' = \frac{1}{\sqrt{n}}\sum_{i=1}^{n} \frac{x_i}{\sigma_w(\xi_i)} \ . \tag{6}$$

This value is an approximation of the result of Kirchhoff migration according to equation (1) with the weight function given by

$$W(M,\xi) = \frac{\sqrt{n}}{\sigma_w(\xi)}. \tag{7}$$

Note that J_w^* follows the student distribution as suggested by Landa et al. (1987) if we use $w = n/2$. Moreover, a window of approximately the size of the Fresnel aperture leads to a good enhancement of the diffraction against a suppression of the reflections (see Figures 3 and 4).

NUMERICAL EXPERIMENTS

We have implemented and tested the above diffraction imaging techniques for a few simple synthetic models. Below, we report the general results using two of these examples.

Model with three diffractors

The first model consists of two diffraction points and one dipping reflector with an endpoint in the center of the model, buried in a constant-velocity background with $v = 2000$ m/s (see Figure 5).

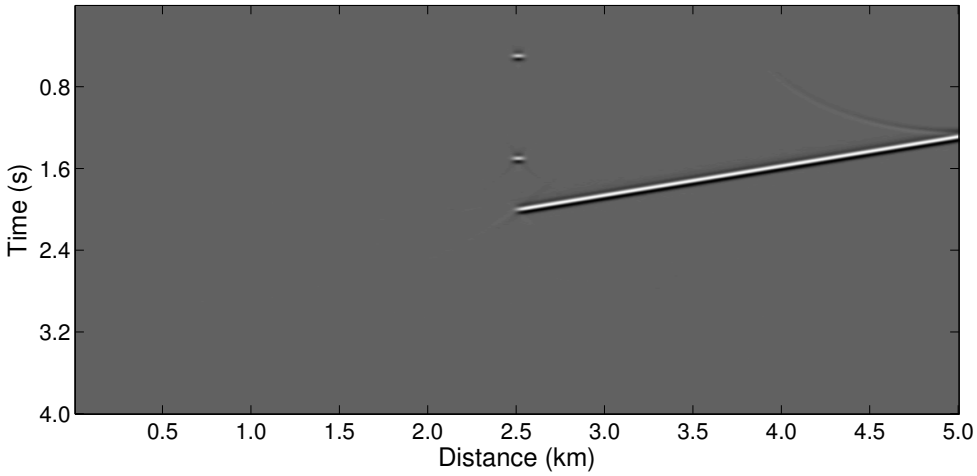

Figure 7: Time-migrated image of dataset from Figure 6.

The synthetic dataset was generated by Kirchhoff modelling. It simulates a zero-offset section with 500 source-receivers pairs spaced at 10 m covering an extension of 5000 m. To the synthetic data we added random noise with a signal-to-noise ratio (S/N) of 100 with respect to the reflection event, which corresponds to a S/N of about 10 for the diffraction events (see Figure 6).

Conventional Kirchhoff migration of these data produces the image shown in Figure 7. While this image contains all three diffraction points, the two isolated diffraction points have rather low amplitudes and would be hard to visualize in noisy data. Only the endpoint of the reflector is clearly identifiable as a diffraction point. Figure 8 shows the diffraction operators of image locations associated to (a) a void ($x = 2.5$ km, $t = 0.8$ s), (b) a reflection ($x = 3.5$ km, $t = 1.73$ s) and (c) a diffraction ($x = 2.5$ km, $t = 0.5$ s) point, respectively.

As suggested by Landa et al. (1987), we normalize the dataset trace-by-trace using its envelope (see Figure 9). Figure 10 shows the diffraction panels for the profile located at $x = 2.5$ km obtained from the raw data and from the normalized data. The diffraction amplitudes (flat events) are equalized to the reflections (other events).

We started by devising a kNN classifier for this data set. As mentioned above, for our purpose of imaging diffractions it is sufficient to use only two classes ($N = 2$): the diffraction class C_0 and the non-diffraction class C_1 (that includes both reflection and void image points). To train the kNN classifier, we used the diffraction operators evaluated at the two isolated point diffractors as training patterns for the diffraction class. The training patterns for the non-diffraction class were the diffraction operator at several locations, including reflector and void image points.

We then applied the so-trained kNN classifier to the diffraction operators of the whole normalized dataset. The result is depicted in Figure 11. We see that the method has correctly identified and positioned all three diffractor points in the model, i.e., the two isolated point diffractors used for the training and also the tip of the reflector not used in the training process, and has not misidentified any additional points as diffractions.

For diffraction imaging using the statistical approach, we calculated the variance σ_{50} for the diffraction operators of the whole normalized dataset and used it as weight function in the Kirchhoff migration operation (1). The resulting section is depicted in Figure 12. We see that also the statistical approach has correctly identified and positioned all three diffractors. However, two of the three diffractor points present a rather weak amplitude, so that they might be hard to spot in noisy data. The method also presents false positives. Additional points close to the boundaries were misidentified as diffractors. Finally note that the statistical approach presents lower resolution of the diffractors as compared to the kNN classifier approach.

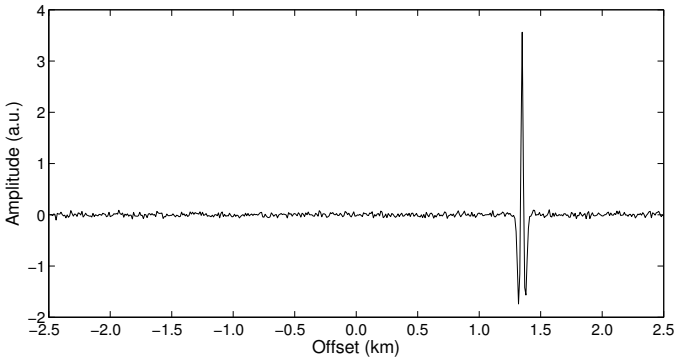

(a)

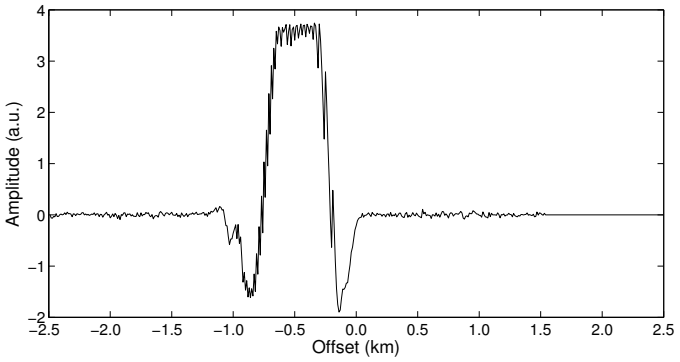

(b)

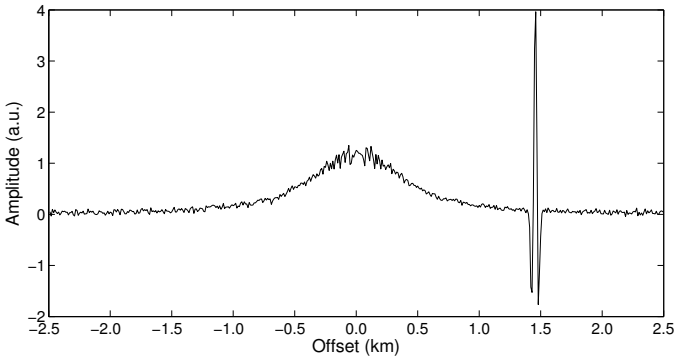

(c)

Figure 8: Diffraction operators of image locations in Figure 7 associated to (a) a void ($x = 2.5$ km, $t = 0.8$ s), (b) a reflection ($x = 3.5$ km, $t = 1.73$ s) and (c) a diffraction ($x = 2.5$ km, $t = 0.5$ s) point.

Model with thirteen diffractors

For a more meaningful test, we applied then both methods to a more complex model consisting of 13 diffraction points. There are 4 isolated point scatterers at depths 0.3 km and 0.5 km, 4 tips of reverse faults at 0.7 km and 1.0 km, and 5 tips of normal faults at 2.0 km and 2.3 km depth (see Figure 13). They are buried in a constant-velocity background with $v = 2000$ m/s covering an extension of 8 km in the x direction. The maximum depth of the model is 4 km.

Again, we generated the zero-offset data by Kirchoff modelling, this time using 800 source-receiver pairs spaced by 10 m with a Ricker wavelet of dominant frequency 12 Hz. Additionally, we added random noise with a signal-to-noise ratio of 100. The generated data and its time-migrated image are depicted in Figures 14 and 15. While the edge diffractors are clearly identifiable in the migrated image in Figure 15, the resolution is insufficient to clearly distinguish the point diffractors at the top of the model.

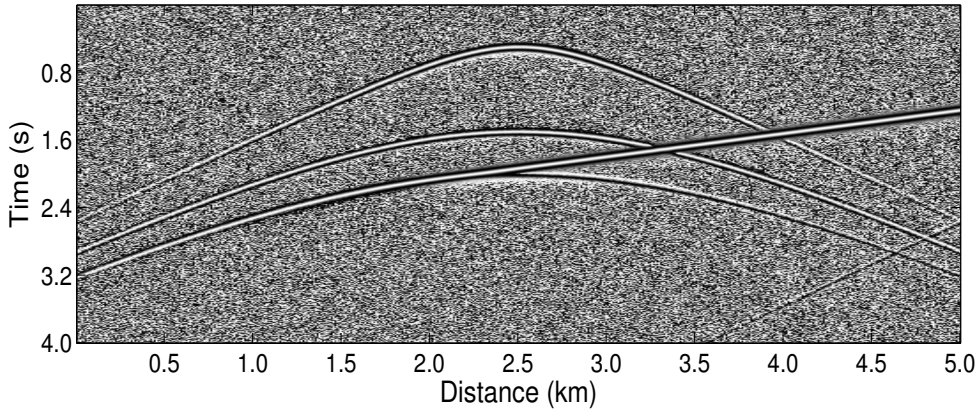

Figure 9: Normalized dataset.

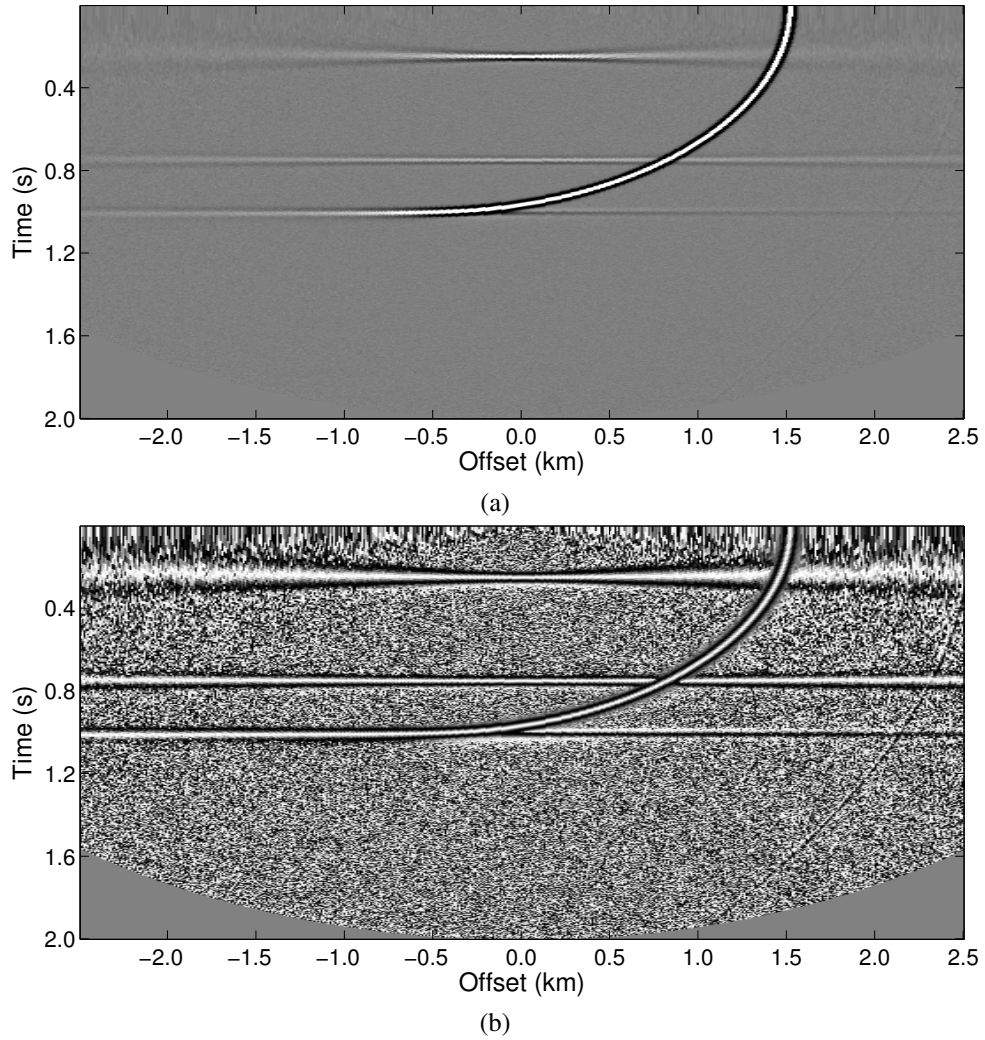

Figure 10: Diffraction panels at 2.5 km obtained from the (a) raw data and (b) normalized data.

Figure 16 shows the result of both diffraction imaging methods. For the pattern-recognition approach, we used the kNN classifier trained on the first model as described above. The kNN classifier correctly identified all 13 diffraction points. The point diffractors are clearly resolved. On the other hand, in the

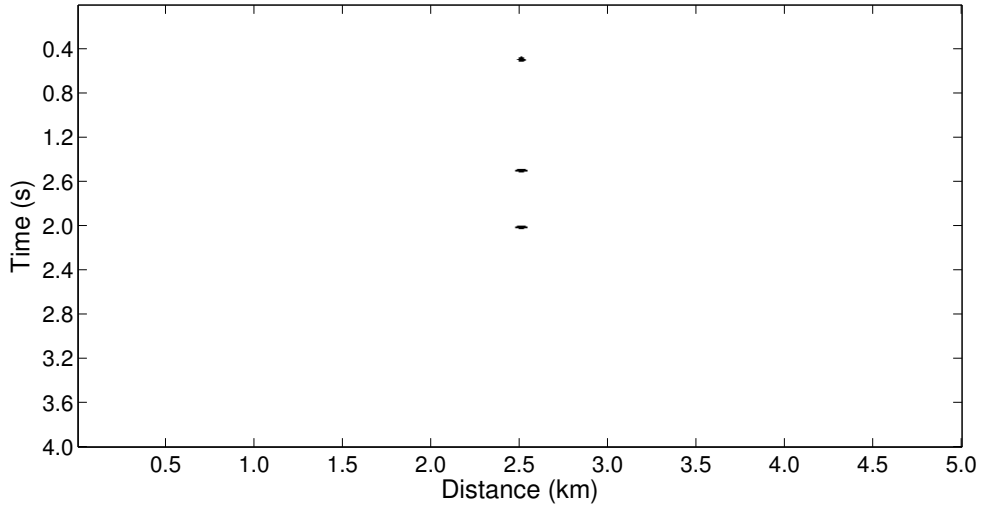

Figure 11: Image points classified as belonging to the diffraction class by the kNN classifier.

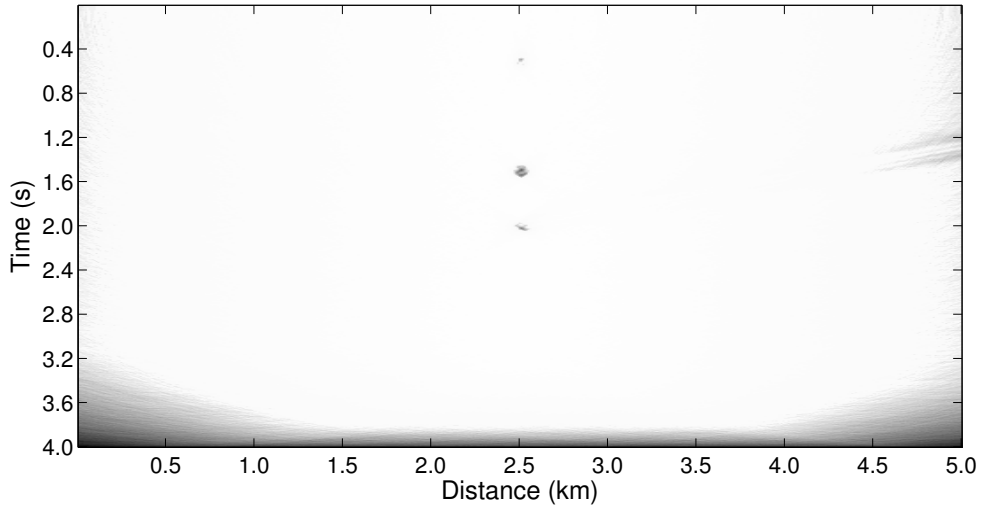

Figure 12: Kirchhoff migration using weights from the statistical analysis over the diffraction operator curves.

image obtained with the statistical method, only the edge diffractions from the tips of the normal and reverse faults are visible, but none of the point scatterers. While an analysis of the numerical values in the image reveals that the point scatterers are actually imaged by the method, their amplitudes are too low to show up in the image. Moreover, as for the first model, the resolution of the image from the statistical method is inferior to that of the kNN classifier. It is important to note that in both methods the location of the diffractions generated by the normal faults have lower resolution when compared to the others (some smearing can be seen). Other numerical tests (not shown here) indicate that this resolution loss is systematic and can be related to the faults' dip.

CONCLUSIONS

In this work we used the diffractor operator proposed by Tabti et al. (2004) as a tool for diffraction imaging. One straightforward approach was its use in a pattern recognition technique to identify and distinguish diffraction events from reflection events and noise areas by their amplitude pattern. Another approach

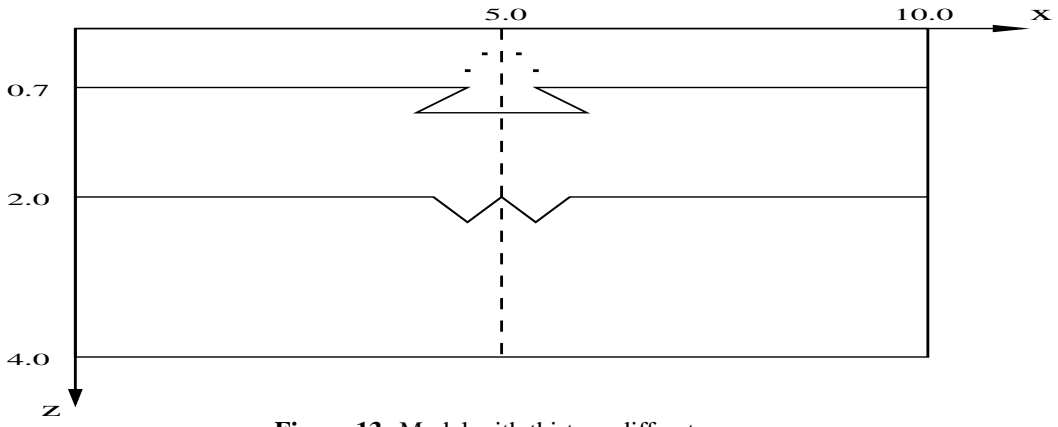

Figure 13: Model with thirteen diffractors.

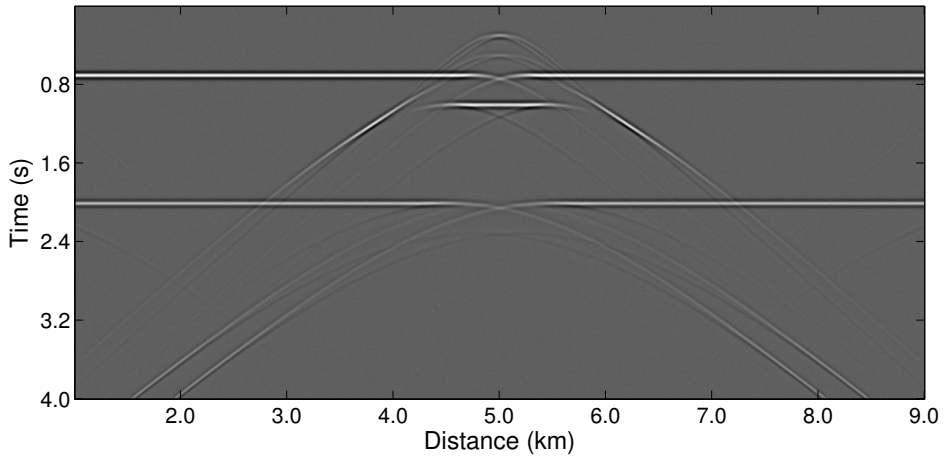

Figure 14: Synthetic zero-offset data for the model of Figure 13.

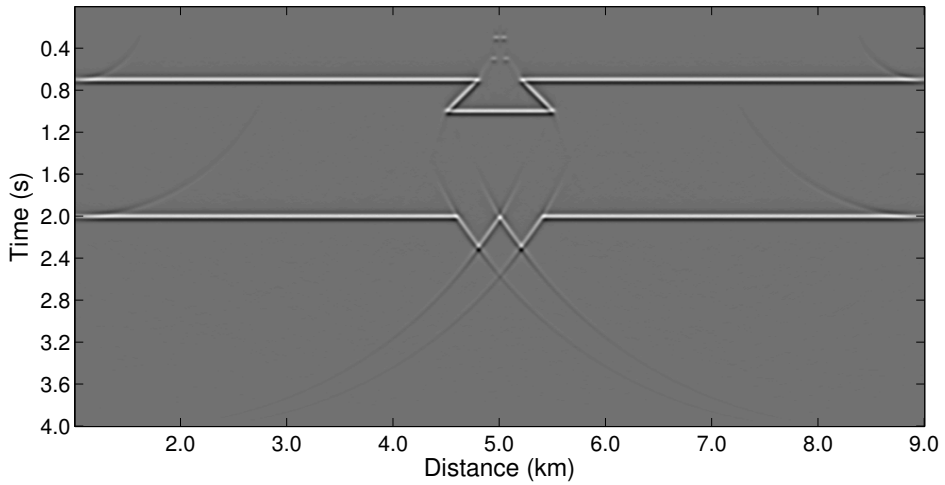

Figure 15: Time-migrated image of the data in Figure 10.

consists in performing a statistical analysis of the amplitude behaviour along each diffraction operator to determine stacking weights for Kirchhoff migration that enhance diffractions and reduce reflections.

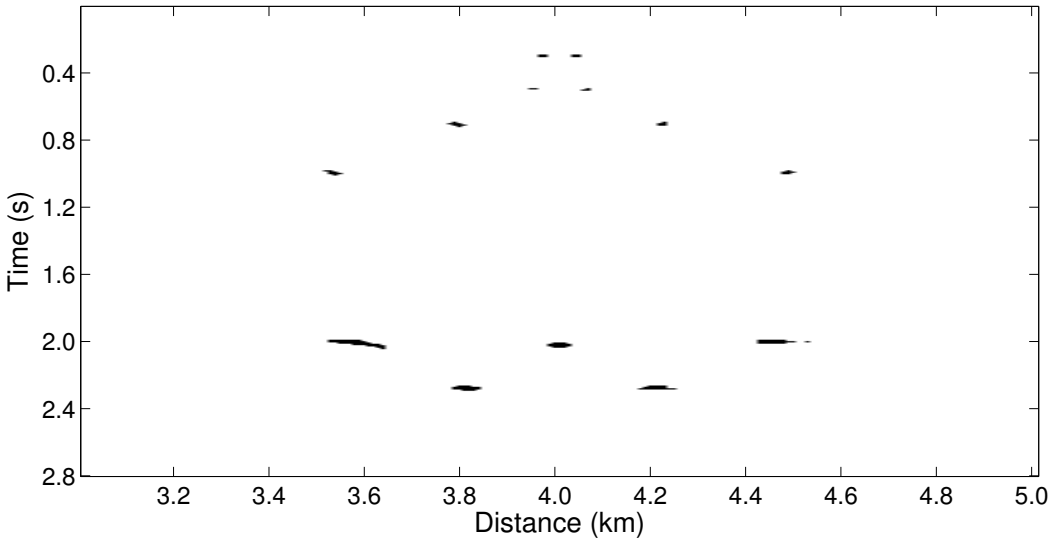

(a)

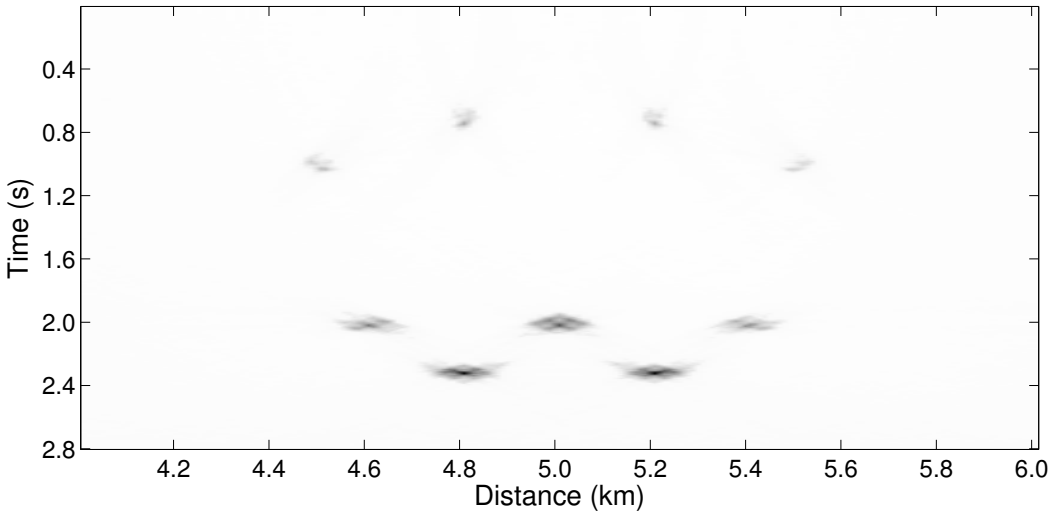

(b)

Figure 16: Diffraction locations by (a) kNN classifier and (b) Kirchhoff migration using the variance σ_{50} as a weight.

In preliminary numerical experiments, the approach based on the k-nearest-neighbours (kNN) classifier showed promising results. After training with selected diffraction operators pertaining to a synthetic data set from a very simple synthetic model, the kNN classifier was able to correctly detect all diffraction points in a considerably more complicated model, not missing a single point and not creating a single false positive. The statistical approach can be recommended for the detection of edge diffractions, but had difficulties to attribute sufficient amplitude to point diffractors. Moreover, it suffers from less resolution and more boundary effects.

Further investigations are necessary to evaluate the robustness and tolerance of new approach with respect to more complicated geological settings and higher noise levels, and whether the performance can be improved by combining the methods. Other possible improvements of the pattern-recognition method might be achieved by replacing the simple kNN classifier by other, more sophisticated classifiers, such as the support vector machine (SVM), the neural network, or the decision tree (Bishop, 1995, 2006; Breiman et al., 1984). An improvement possibility for the statistical approach is to measure the variation of the

Fresnel aperture with the signal's frequency, because this property varies for reflections and remains constant for diffractions. Beyond amplitude analysis, the diffraction panel illustrated in Figure 10 suggests the application of a dip-filtering technique as another possibility for imaging diffractions.

REFERENCES

Bishop, C. (1995). *Neural Networks for Pattern Recognition*. Oxford University Press, Oxford, UK.

Bishop, C. M. (2006). *Pattern Recognition and Machine Learning (Information Science and Statistics)*. Springer-Verlag New York.

Breiman, L., Friedman, J. H., Olshen, R. A., and Stone, C. (1984). *Classification and Regression Trees*. Chapman & Hall, New York, NY.

Duda, R. and Hart, P. (1973). *Pattern Classification and Scene Analysis*. John Wiley & Sons, New York, NY.

Halliburton (2001). Basic petroleum geology and log analysis. Halliburton Company.

Landa, E. and Keydar, S. (1998). Seismic monitoring. *Geophysics*, 63.

Landa, E., Shtivelman, V., and Gelchinsky, B. (1987). A method for detection of diffacted waves on commom-offset sections. *Geophysical Prospecting*, 35.

Moser, T. and Howard, C. (2008). Diffraction imagining in the depth. *Geophysical Prospecting*, 56.

Schleicher, J., Hubral, P., Tygel, M., and Jaya, M. S. (1997). Minimum apertures and Fresnel zones in migration and demigration. *Geophysics*, 62(2):183–194.

Schleicher, J., Tygel, M., and Hubral, P. (1993). 3-D true-amplitude finite-offset migration. *Geophysics*, 58(8):1112–1126.

Tabti, H., Gelius, L.-J., and Hellmann, T. (2004). Fresnel aperture prestack depth migration. *First Break*, 22.

Theodoridis, S. and Koutroumbas, K. (1999). *Pattern Recognition*. Academic Press.

Zhu, X. and Wu, R.-S. (2010). Imaging diffraction points using the local image matrices generated in prestack migration. *Geophysics*, 75(1).